*Nucleic Acids Research*, 2026, **54**, gkaf1421
https://doi.org/10.1093/nar/gkaf1421
**RNA and RNA-protein complexes**

# Mechanistic insights into Lin28-dependent oligo-uridylylation of pre-let-7 by TUT4

**Xiaojie Han, Seisuke Yamashita*, Kozo Tomita***

Department of Computational Biology and Medical Sciences, Graduate School of Frontier Sciences, The University of Tokyo, Kashiwa, Chiba 277-8562, Japan

*To whom correspondence should be addressed. Email: yamashita-s@edu.k.u-tokyo.ac.jp
Correspondence may also be addressed to Kozo Tomita. Email:kozo-tomita@edu.k.u-tokyo.ac.jp

## Abstract

Lin28-dependent oligo-uridylylation of precursor let-7 (pre-let-7) by terminal uridylyltransferases 4 and 7 (TUT4/7) represses let-7 expression by blocking Dicer processing, thereby regulating cell differentiation and proliferation. The interaction between the Lin28:pre-let-7 complex and the N-terminal Lin28-interacting module (LIM) of TUT4/7 is required for pre-let-7 oligo-uridylylation by the C-terminal catalytic module (CM). Here, we report the cryogenic electron microscopy structure of human TUT4 complexed with Lin28A and oligo-uridylated pre-let-7, representing the elongation stage of oligo-uridylylation. Structural and biochemical analyses suggest that, after recruitment of pre-let-7 to the LIM through interactions between its terminal stem-loop and Lin28A, the CM associates with the LIM through protein–protein interactions. The double-stranded stem region of pre-let-7 is surrounded by the CM and LIM, the upper portion of the duplex unwinds, and the 3′ end of pre-let-7 is positioned in the CM catalytic site for the initiation of oligo-uridylylation. At the oligo-uridylylation stage, the CM finger domain clamps the double-stranded region of pre-let-7, thereby further stabilizing the pre-let-7:TUT4 complex, enabling processive elongation of the uridine tail by the CM. Thus, the LIM functions as a stable anchor, working together with Lin28A to ensure efficient and processive oligo-uridylylation of pre-let-7.

## Graphical abstract

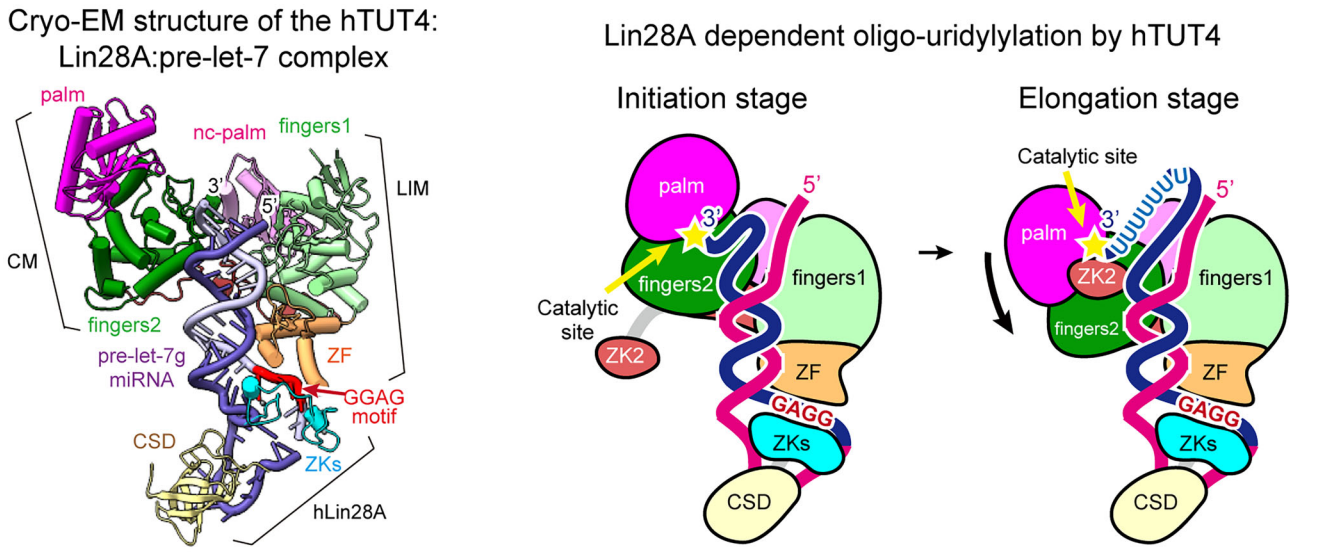


## Introduction

The let-7 family of microRNAs (miRNAs) is evolutionarily and functionally conserved from nematodes to humans [1, 2]. By binding to the 3′ untranslated regions (UTRs) of target mRNAs, it suppresses their translation and thereby regulates key biological processes such as stem cell differentiation, developmental timing, and tumor suppression [3–5]. Down-regulation of let-7 has been observed in many human cancers, where it contributes to uncontrolled cell proliferation [6].

The biogenesis of the let-7 family follows the canonical miRNA pathway. Primary transcripts (pri-let-7) are synthesized by RNA polymerase II [7] and processed by Drosha and

**Received:** September 22, 2025. **Revised:** November 23, 2025. **Accepted:** November 26, 2025

its cofactor DGCR8 into precursor let-7 (pre-let-7) in the nucleus [8]. Pre-let-7, ∼70–80 nucleotides long, is classified into two groups: group I with a 2-nt 3′ overhang and group II with a 1-nt 3′ overhang. Pre-let-7 is exported to the cytoplasm via the Exportin-5/Ran-GTP complex [9] and then cleaved by the RNase III enzyme Dicer to yield mature let-7 miRNA. The mature miRNA is incorporated into the RNA-induced silencing complex (RISC), where it functions in gene silencing through translational repression or mRNA degradation [10].

One of the key regulators of let-7 biogenesis is the RNA-binding protein Lin28A, which is abundantly expressed in embryonic stem cells and cancer cells but downregulated in differentiated cells. Lin28A and let-7 exhibit an inverse expression pattern *in vivo*, reflecting their opposing biological roles. Lin28A not only regulates developmental timing and reprogramming to induced pluripotent stem (iPS) cells but is also implicated in cancer progression, inflammation, and metabolism [5].

Mechanistically, Lin28A controls let-7 biogenesis through interaction with the terminal uridylyl transferases (TUTases) [11–16], TUT4 and TUT7, which are members of the terminal nucleotidyl transferase (TENT) family [17–19], and distinct from U6-specific TUTase, TUT1 [19–21]. In the presence of Lin28A, group I and group II pre-let-7 molecules are bound at a conserved sequence in the terminal loop, recruiting TUT4/7 to add 3′-oligo-uridine tails. The binding of Lin28A to pre-let-7 and the oligo-uridylylation of pre-let-7 by TUT4/7 block subsequent Dicer processing and target pre-let-7 for degradation by the 3′-to-5′ exonuclease Dis3l2 [22–24], thereby repressing mature let-7 expression. In contrast, in the absence of Lin28A, TUT4/7 catalyzes mono-uridylylation of group II pre-let-7, converting them into optimal Dicer substrates with 2-nt 3′-overhang and promoting efficient maturation [15]. Thus, TUT4/7 exerts a dual regulatory role, functioning as positive or negative factors in let-7 biogenesis depending on Lin28A expression (cell type) and the structure of the pre-let-7 3′ end (group I or II: 2-nt or 1-nt overhang). The balance between Lin28 and let-7, modulated by TUT4/7, therefore acts as a molecular switch governing cell fate decisions, development, and tumorigenesis [5].

Lin28A consists of an N-terminal cold shock domain (CSD) and C-terminal tandem zinc knuckles (ZKs). The molecular basis of the interaction between Lin28 and pre-let-7 has been well characterized [25–27]. The CSD binds to the 5′-GXGAY-3′ motif in the terminal stem-loop structure of pre-let-7 (the pre-element, preE), and the ZKs bind to a conserved 5′-GGAG-3′ motif near the 3′ end of preE [26, 28]. TUT4/7 has a multidomain structure consisting of an N-terminal Lin28-interacting module (LIM) and a C-terminal catalytic module (CM), linked via a flexible linker [29]. The CM is responsible for nucleotidyltransferase activity, while the LIM mediates interaction with the Lin28:pre-let-7 complex [14]. During Lin28-dependent oligo-uridylylation of pre-let-7 by TUT4/7, Lin28A and pre-let-7 interact with the LIM to form a ternary complex [30]. This interaction is pre-let-7–dependent, and the ZKs of Lin28A are necessary and sufficient for ternary complex formation among TUT4/7, Lin28, and pre-let-7 [31].

Structural studies of the CM of human TUT7 bound to RNA suggest a mechanism for mono-uridylylation of group II pre-let-7 and reveal the involvement of the CM ZKs in RNA oligo-uridylylation [32]. In the absence of Lin28, pre-let-7 does not stably interact with TUT7, and 3′ ends with more than a 2-nt overhang cannot be accommodated by the CM. Thus, TUT4/7 preferentially catalyzes mono-uridylylation of group II pre-let-7 and releases the product. In the presence of Lin28, however, pre-let-7 stably interacts with TUT4/7. After several UMP additions to the 3′ end within the CM, the ZK in the CM recognizes the single-stranded oligo(U) tail, stabilizing it in the catalytic pocket and enabling processive, efficient oligo-uridylylation. Furthermore, structural and functional studies of the LIM of human TUT4 show that its zinc finger (ZF) binds the double-stranded region of pre-let-7, thereby stabilizing the TUT4:Lin28:pre-let-7 ternary complex and enhancing oligo-uridylylation by the CM [29]. Recently, cryogenic electron microscopy (cryo-EM) structures of human TUT7 in complex with pre-let-7 containing a 1-nt 3′ overhang (pre-let-7g), in the presence or absence of Lin28A, were reported [33]. Despite the modest resolution, these structures suggested possible transition mechanisms of TUT7-mediated mono-uridylylation in the absence of Lin28A and oligo-uridylylation in its presence. However, the detailed mechanism by which the two distinct domains, LIM and CM, of TUT4/7 coordinate Lin28A-dependent oligo-uridylylation of pre-let-7 has not been fully understood. In particular, the mechanism underlying Lin28A-dependent elongation of oligo-uridylylation of pre-let-7 by TUT4/7 remains elusive.

Here, we present the cryo-EM structure of the TUT4:Lin28A:oligo-uridylylated pre-let-7 complex, representing the oligo-uridylation stage. Our cryo-EM and biochemical analyses, together with comparisons to the TUT7:Lin28A:pre-let-7 structure available, provide the possible processive mechanism for Lin28-dependent oligo-uridylylation of pre-let-7 by TUT4/7.

## Materials and methods

### Plasmid construction

Plasmids expressing truncated human TUT4 (hTUT4_mini) and full-length hLin28A were prepared as described previously [29]. Briefly, synthetic DNA fragments encoding human TUT4 (amino acid residues 1–1375) and Lin28A (amino acid residues 1–209) were purchased from Takara Bio (Japan) and GeneCopoeia, respectively (Supplementary Table S1). PCR-amplified fragments encoding hTUT4_mini (amino acid residues 202–1313) or full-length hLin28A were cloned into the NdeI and XhoI sites of pET29a or pET28b (Merck Millipore, Japan), respectively. Amino acid sequences of recombinant hTUT4 and hLin28A are provided in Supplementary Table S2. Mutant constructs of hTUT4 and hLin28A were generated by inverse PCR. The hTUT4_281–1313 construct was cloned into the NdeI and XhoI sites of pET29a. Oligonucleotides used for cloning and mutagenesis are listed in Supplementary Table S3.

### Expression and purification of recombinant proteins

*Escherichia coli* BL21(DE3) (Novagen, Japan) was transformed with plasmids expressing hTUT4, hLin28A, or their variants, and cultured in LB medium containing 50 μg/mL kanamycin at 37°C until the OD660 reached 0.8. Protein expression was induced with 0.1 mM isopropyl-β-D-thiogalactopyranoside (IPTG), followed by incubation at 18°C for 16 h. For hTUT4_mini purification, harvested cells were lysed in buffer containing 20 mM Tris–HCl, pH 7.0, 500 mM NaCl, 10 mM β-mercaptoethanol, 20 mM imi-

dazole, 0.1 mM phenylmethylsulfonyl fluoride (PMSF), and 5% (v/v) glycerol. Proteins were purified sequentially by Ni-NTA affinity (QIAGEN, Japan), HiTrap Heparin HP (GE Healthcare, Japan), and HiLoad 16/60 Superdex 200 size-exclusion chromatography (GE Healthcare, Japan) in buffer containing 20 mM Tris–HCl, pH 7.0, 200 mM NaCl, and 10 mM β-mercaptoethanol. The proteins were concentrated and stored at –80°C. hLin28A was purified similarly, with an additional HiTrap Q step (GE Healthcare, Japan) after Ni-NTA chromatography to remove nucleic acids. Protein purity for structural and biochemical analyses was confirmed by Sodium dodecyl-sulfate polyacrylamide gel electrophoresis (SDS-PAGE) (Supplementary Fig. S1).

### RNA synthesis and preparation

Plasmids containing pre-let-7 genes were purchased from Eurofins (Japan), with a T7 promoter placed upstream. For transcription of pre-let-7 miRNAs beginning with a 5′-uridine, a hammerhead ribozyme was inserted between the T7 promoter and the pre-let-7 gene [34]. Synthetic gene and RNA sequences are listed in Supplementary Tables S4 and S5. Pre-let-7 and variants were synthesized by *in vitro* transcription using T7 RNA polymerase and PCR-amplified DNA templates. To obtain homogeneous 3′ ends, reverse primers with two or three terminal 2′-O-methylated nucleotides [35], purchased from Eurofins, were used (Supplementary Table S6). RNAs were phenol–chloroform extracted and purified by gel extraction (for pre-let-7g with three additional 3′ uridines: pre-let-7g_UUU) or by HiTrap Q HP (GE Healthcare, Japan) for uridylylation assays. RNAs were ethanol-precipitated, dissolved in water, and stored at –30°C.

### Cryo-EM grid preparation and data collection

The hTUT4_mini:Lin28A:pre-let-7g_UUU complex was reconstituted by mixing equimolar amounts (26.5 μM each) of the three components, followed by purification on a Superdex 200 Increase 10/300 column (GE Healthcare, Japan) in buffer containing 20 mM Tris–HCl, pH 7.0, 200 mM NaCl, 2 mM $MgCl_2$, and 10 mM β-mercaptoethanol. Fractions containing all three components were concentrated and stored at –80°C. Before grid preparation, samples were adjusted to 0.7 mg/mL with 0.005% (v/v) Tween-20. Quantifoil Cu R1.3/1.2 #300 and UltrAuFoil #300 grids (Quantifoil) were glow-discharged for 30 s at 8 mA using a PIB-10 (Vacuum Device). Aliquots (3 μL) were applied to grids at 4°C and 100% humidity, blotted with a force of 10 for 4 s, and plunge-frozen in liquid ethane using a Mark IV Vitrobot (Thermo Fisher Scientific).

Cryo-EM data were collected on a Titan Krios G4 microscope (Thermo Fisher Scientific) operating at 300 kV and equipped with a GIF Quantum-LS energy filter and a K3 Summit direct electron detector (Gatan, Inc.). Images were recorded at a pixel size of 0.83 Å (nominal magnification ×105 000) with a total exposure of 50 $e^-/Å^2$ and a defocus range of –0.8 to –1.8 μm. Five datasets were collected and merged: three using Quantifoil Cu R1.3/1.2 #300 grids (4296, 9977, and 9818 movies) and two using UltrAuFoil #300 grids (6382 and 7290 movies).

### Image processing

The cryo-EM data were processed using CryoSPARC (version 4.6.0) [36]. Movie stacks were subjected to motion correction [37] and contrast transfer function (CTF) estimation. Particles were picked, classified in 2D, and further polished by reference-based motion correction. All particles were then merged and separated into two groups by 2D classification based on the presence or absence of density corresponding to the C-terminal CM of hTUT4 (conformations 1 and 2, respectively). Focused 3D classification with a mask covering the hLin28A region yielded particle sets displaying distinct blob-shaped density corresponding to the CSD of hLin28A. Final nonuniform refinement [38] of these CSD-containing particles produced maps at 3.78 Å (conformation 1, with CM) and 3.82 Å (conformation 2, without CM). The maps were post-processed with EMReady [39] and used for model building and figure preparation. The data-processing workflow, map validation, and representative cryo-EM images are shown in Supplementary Figs S2–S4.

### Model building and refinement

For the hTUT4:Lin28A:pre-let-7_UUU complex, the cryo-EM map was initially fitted with the hTUT4:pre-let-7g structure (PDB ID: 8OST) [33], the AlphaFold3-predicted model [40] of the hTUT4 CM, and the mouse Lin28A:pre-element of pre-let-7g structure (PDB ID: 3TS2) [32]. The model was subsequently rebuilt in Coot [41] and refined using Phenix.refine [42]. Cryo-EM data collection and refinement statistics are provided in Supplementary Table S7. Figures were generated with UCSF ChimeraX (version 1.9) [43].

### *In vitro* uridylylation

A 30-μl reaction mixture containing 50 mM Tris–HCl, pH 8.5, 100 mM NaCl, 10 mM $MgCl_2$, 10 mM β-mercaptoethanol, 1 mM UTP, 250 nM pre-let-7 miRNA (and its variants), and 20 nM hTUT4 (or its variants) was incubated at 37°C in the presence or absence of 500 nM hLin28A (or its variants) [29]. Under the reaction condition, the oligo-uridylylation of pre-let-7 does not proceed in the absence of Lin28, and around 30–40 uridines are added to the 3′-end of pre-let-7, as previously described (Supplementary Fig. S1) [11, 29]. The longer tails observed in the extended reaction likely result from a partially distributive elongation mechanism, in which hTUT4 can transiently unbind and re-bind to the oligo-uridylated RNA substrate, thereby enabling further extension in Lin28-independent manner.

At the indicated time points, 5-μl aliquots were withdrawn and the reaction was terminated. RNAs were resolved by 10% (w/v) denaturing polyacrylamide gel electrophoresis and stained with ethidium bromide. Bands were visualized and quantified using a Gel Doc EZ system and Image Lab software (Bio-Rad, Japan).

## Results

### Cryo-EM analysis of the hTUT4:hLin28A:pre-let-7g_UUU complex

To clarify the molecular basis of pre-let-7 oligo-uridylylation by TUT4 in the presence of Lin28A, we performed cryo-EM analysis of the ternary complex comprising TUT4, Lin28A, and pre-let-7. Human TUT4 and TUT7 (hTUT4/7) are multi-domain proteins composed of an N-terminal Lin28-binding module (LIM) and a C-terminal catalytic module (CM), connected via a flexible linker (Fig. 1A) [19].

The LIM consists of a noncatalytic nucleotidyltransferase domain (NTD1) and a ZF, and functions to bind both

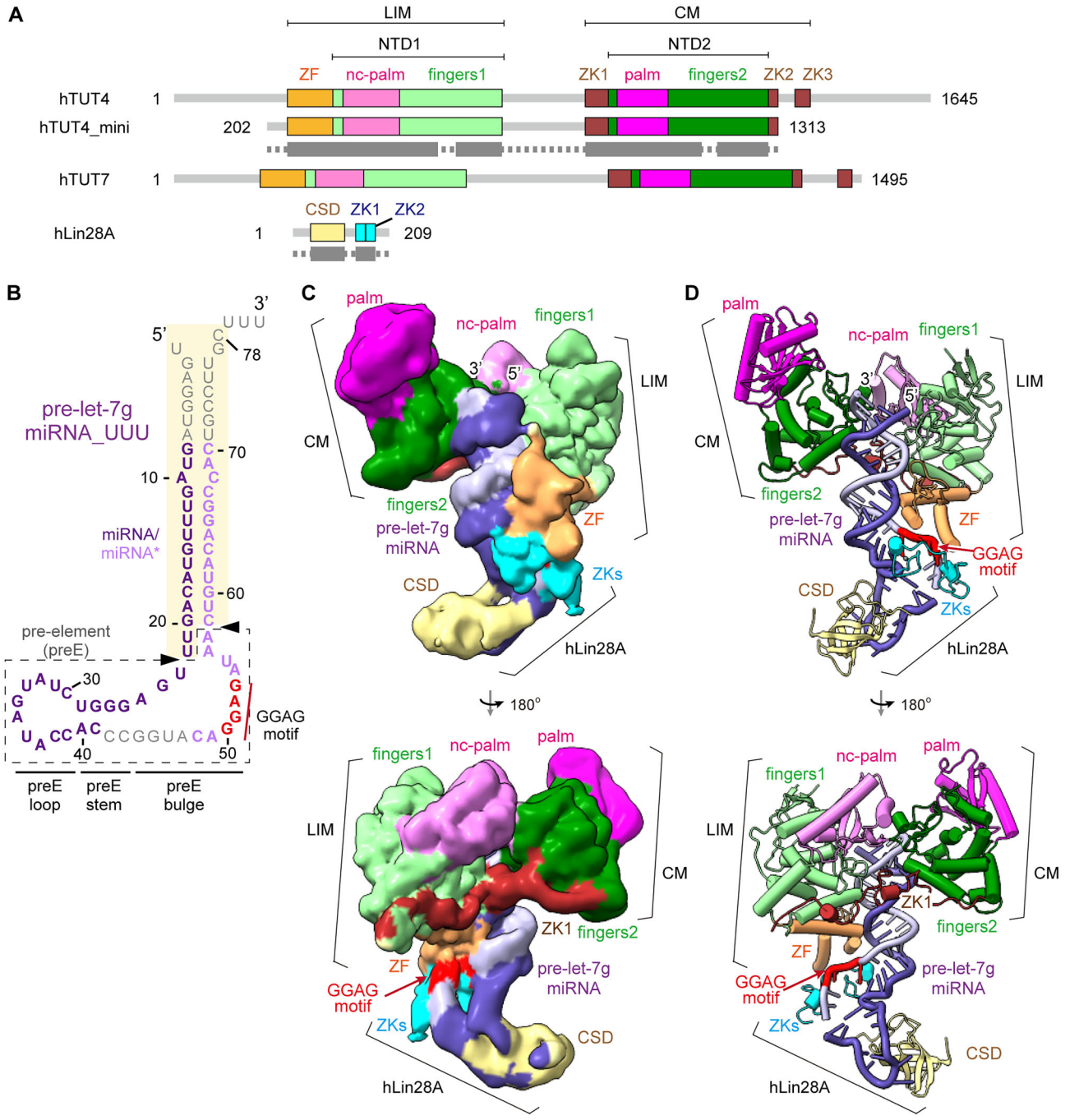


**Figure 1.** Overall structure of the hTUT4_mini:hLin28A:pre-let-7g_UUU. (**A**) Domain organization of hTUT4, hTUT4_mini (residues 202–1313), hTUT7, and hLin28A. ZF, nc-palm, fingers1, ZK, palm, and fingers2 of hTUT4/7 are shown in orange, light magenta, light green, brown, magenta, and green, respectively. The CSD and ZKs of hLin28A are colored yellow and cyan. Modeled regions are indicated by gray rectangles, and unmodeled regions by dashed lines. (**B**) Secondary structure of pre-let-7g_UUU (U1–C78 plus three additional 3′ uridines, 81 nt total). The GGAG motif (G50–G53) is highlighted in red. The 5′ and 3′ halves are shown in purple and light purple, respectively, with unmodeled regions in gray. Dicer cleavage sites are indicated by black arrowheads, the miRNA/miRNA∗ duplex is highlighted in yellow, and the preE is outlined with a dashed line. (**C**) Cryo-EM density map of the hTUT4_mini:hLin28A:pre-let-7g_UUU complex. (**D**) Cartoon representation of the overall structure, with domains colored as in (A, B). Several regions were not modeled due to poor cryo-EM map densities. The following residues are not modeled. In hTUT4: residues 1–273, 574–612, 714–894, 1147–1181, 1278–1313, and the C-terminal His-tag. In hLin28A: residues 1–34, 123–135, 178–209, and the His-tag. In pre-let-7g: nucleotides 1–7, 42–47, and 71–81. Cryo-EM data collection and refinement statistics are provided in Supplementary Table S7.

pre-let-7 and Lin28A. The CM consists of a nucleotidyltransferase domain (NTD2) and three zinc knuckles (ZK1–3), forming the catalytic site for uridylylation of the 3′ end of pre-let-7. Both NTD1 and NTD2 are further subdivided into palm and fingers domains (Fig. 1A). While NTD2 in CM is responsible for the uridylylation reaction, NTD1 in LIM is noncatalytic due to mutations in the catalytic carboxylates [29]. Previous studies have shown that a truncated form of hTUT4 (amino acid residues 202–1313; hTUT4_mini), lacking ZK3 in CM, is capable of Lin28-dependent oligo-uridylation of pre-let-7 and formation of the TUT4:Lin28A:pre-let-7 ternary complex [29, 32].

Human Lin28A (hLin28A) consists of an N-terminal cold-shock domain (CSD) and C-terminal zinc knuckles (ZK1 and ZK2), which bind the preE of pre-let-7 (Fig. 1B). The CSD recognizes the 5′-GXGAY-3′ motif in the preE loop, while the ZKs bind the 5′-GGAG-3′ motif in the preE bulge (Fig. 1B). Both ZKs are required for ternary complex formation with pre-let-7 and TUT4 (or TUT7) [25–28].

For structural analysis, we selected pre-let-7g as the RNA substrate. Pre-let-7g, a group-II pre-miRNA with a 1-nt 3′ overhang [15], can be divided into three regions: the 5′-region (nucleotides 1–22), corresponding to the functional miRNA (guide strand) that is incorporated into Argonaute (Ago), the central preE region (nucleotides 23–57), removed by Dicer cleavage, and the complementary region (nucleotides 58–78), corresponding to miRNA∗ (passenger strand) that forms the duplex but is not incorporated into Ago (Fig. 1B). For cryo-EM, we used pre-let-7g with three additional uridines at the 3′ end, hereafter referred to as pre-let-7g_UUU, to capture the uridylylation reaction stage by the TUT4:Lin28A:pre-let-7 complex.

The ternary complex was reconstituted by mixing hTUT4_mini (residues 202–1313), full-length hLin28A, and pre-let-7g_UUU (Fig. 1A and B), followed by purification via size-exclusion chromatography for cryo-EM grid preparation. We collected five datasets, from which particles were picked and then merged into a single particle set for further analysis (Supplementary Fig. S2). 2D classification revealed two types of complexes: one displaying distinct cryo-EM density corresponding to CM (conformation 1), and the other lacking this density (conformation 2). Particles were sorted based on the presence or absence of CM density, and the resulting maps were refined separately. Subsequent 3D classification focusing on the hLin28A region revealed that a subset of particles displayed a distinct blob density corresponding to the CSD of hLin28A. From these particles, we obtained final maps at 3.78 Å resolution (conformation 1) and 3.82 Å resolution (conformation 2) (Supplementary Figs S2–S4 and Supplementary Table S7).

## Overall structure of the hTUT4_mini:hLin28A:pre-let-7g_UUU complex

The structural model of the hTUT4_mini:hLin28A:pre-let-7g_UUU complex was built onto the maps and refined (Fig. 1C and D, Supplementary Table S7, Supplementary Figs S2–S4, and Supplementary movie 1). The two structures, conformation 1 and conformation 2, are almost same except for the presence or absence of CM (Supplementary Fig. S5). The structure with CM (conformation 1) is likely to represent the oligo-uridylylation stage, while the structure without CM density (conformation 2) is likely to represent the substrate binding stage, where the ternary complex is formed by the interactions among LIM of hTUT4, hLin28A, and pre-let-7g, but the 3′-end of pre-let7g is not engaged in the catalytic site in CM. Hereafter, we focus on the conformation 1 structure unless otherwise stated.

In the structural model, several regions of the ternary complex were not modeled due to poor cryo-EM map quality (Fig. 1A and B). In hTUT4, the N-terminal residues (the start methionine and amino acid residues 202–273), the loop in fingers1 (amino acid residues 574–612), the linker between LIM and CM (amino acid residues 714–894), the loop in the fingers2 (amino acid residues 1147–1181), and the C-terminal residues (amino acid residues 1278–1313 and the C-terminal hexa-histidine tag) were not modeled. In hLin28A, the N-terminal residues (amino acid residues 1–34), the linker between CSD and ZKs (amino acid residues 123–135), and the C-terminal residues (amino acid residues 178–209 and the hexa-histidine tag) were not modeled (Fig. 1, and Supplementary Figs S6 and S7). In pre-let-7g, the 5′- and 3′- nucleotides (nucleotides 1–7 and 71–81), and the putative loop in preE (nucleotides 42–47) were not modeled. The statistics for the cryo-EM analysis and structural model refinement are summarized in Supplementary Table S7.

The cryo-EM structure of the hTUT4:hLin28A:pre-let-7g_UUU reveals extensive recognition of pre-let-7g by the multi-domain proteins hTUT4 and hLin28A (Fig. 1C). The RNA double-stranded stem region of pre-let-7g_UUU is accommodated within a cleft formed by the CM and LIM. In particular, ZF and fingers1 in LIM, and ZK1 and fingers2 in CM clamp the double-stranded region of pre-let-7g, as described in detail below. Furthermore, the ZF in LIM and the ZKs of hLin28A together sandwich the 5′-GGAG-3′ motif (G50–G51–A52–G53) of pre-let-7g, and the CSD of hLin28A binds the tip of the pre-let-7g stem loop (preE loop).

The domain architecture is further stabilized by both inter- and intraprotein interactions. The N-terminal and C-terminal regions of ZK1 in CM interact with fingers1 in LIM and fingers2 in CM, respectively. Additionally, the noncatalytic palm (nc-palm) in LIM interacts with fingers2 in CM of hTUT4 (Fig. 1C andD). These interactions position the LIM and CM modules adjacent to each other in the complex, despite being connected by a long flexible linker (Fig. 1A, C, andD). Furthermore, the ZF in LIM directly interacts with the ZKs of hLin28A. Details of these interactions are described below. The 5′- and 3′-terminal dsRNA stems of pre-let-7g were not modeled due to insufficient map density. Likewise, no density was observed for the 3′ end of the RNA in the catalytic pocket of the CM. The map for ZK2 in CM was also not observed. Since ZK2 is reported to interact with the oligo-uridylylated 3′ tail of pre-let-7 [30], it is likely that ZK2 exists in a flexible or mobile state in this complex. This may explain why the 3′ end of the RNA was not observed in the catalytic pocket of the CM.

## Protein–protein interaction in the hTUT4_mini:hLin28A:pre-let-7g_UUU

The overall architecture of the hTUT4 complex is stabilized by extensive interactions between the protein domains (Fig. 2A–E). Fingers1 in LIM interacts with the N-terminal region of ZK1 in CM primarily through a broad network of hydrophobic interactions (Fig. 2A). Hydrophobic residues of ZK1—Tyr898, Val899, Phe900, Ile904, and Leu905—interact with a

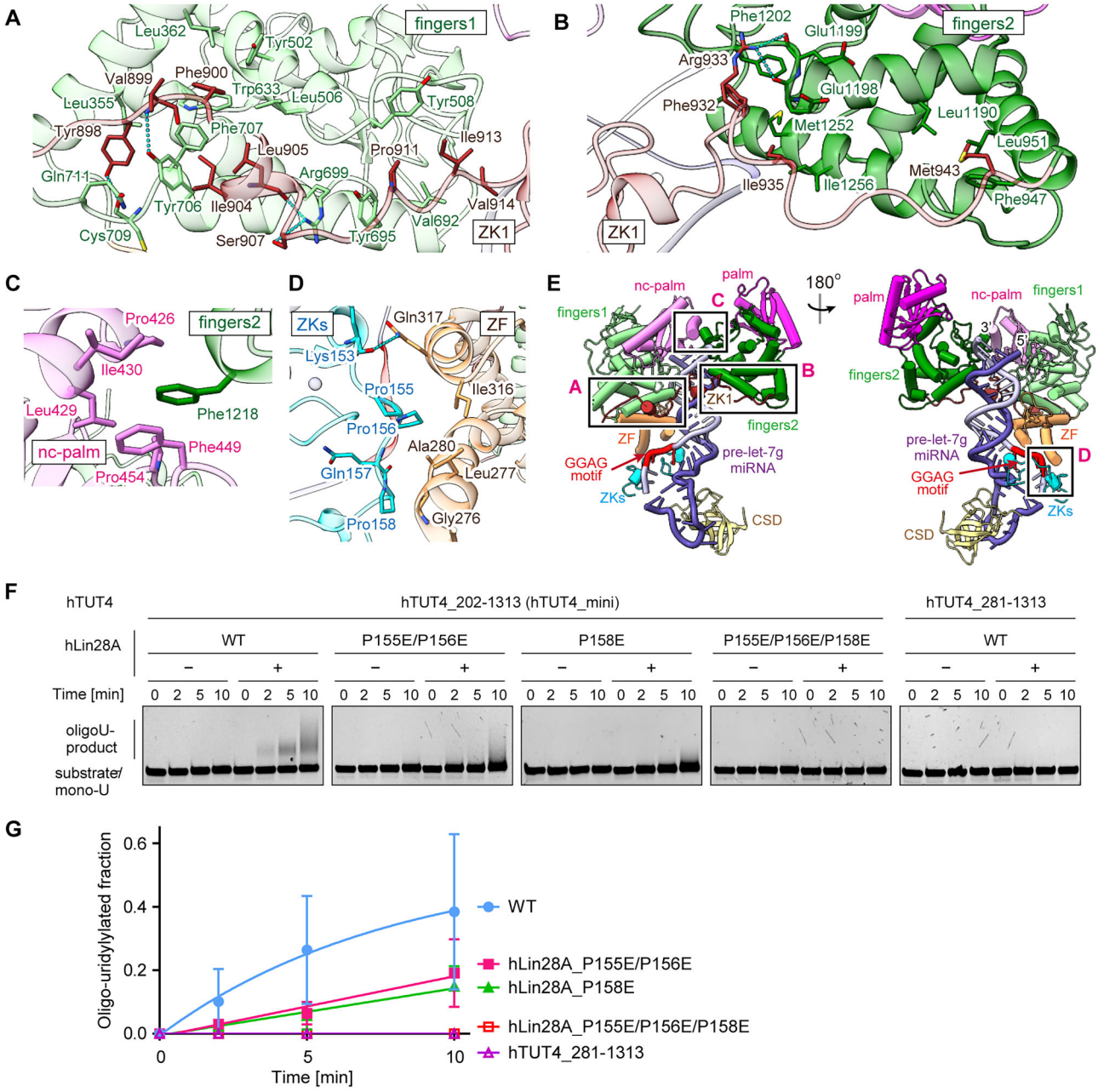


**Figure 2.** Interactions between hTUT4, hLin28A, and pre-let-7g miRNA. (**A–D**) Detailed views of inter-molecular interactions between hTUT4 domains and between hTUT4 and hLIN28A: (A) fingers1 (light green) and ZK1 (brown), (B) fingers2 (green) and ZK1 (brown), (C) nc-palm (light magenta) and fingers2 (green), and (D) hTUT4 ZF (orange) and hLin28A ZKs (cyan). (**E**) Cartoon representation of the overall complex, with regions corresponding to panels (A–D) indicated. (**F**) *In vitro* oligo-uridylylation of pre-let-7a-1 by hTUT4. Substrate RNA (250 nM) was incubated with hTUT4_mini (20 nM) or hTUT4_281–1313 (20 nM) and 1 mM UTP at 37°C, in the presence or absence of hLin28A (500 nM) or its variants. (**G**) Quantification of uridylation activity from (F). Data represent mean ± SD ($n = 3$).

hydrophobic patch on fingers1 composed of Leu355, Gln711, Trp633, Tyr706, Phe707, Leu362, Tyr502, and Leu506. Additionally, Pro911, Ile913, and Val914 of ZK1 form hydrophobic contacts with Tyr695, Tyr508, and Val692 of fingers1. Several hydrophilic interactions further reinforce the binding: Tyr898 in ZK1 forms a hydrogen bond with the main chain oxygen of Cys709 in fingers1; Tyr706 in fingers1 hydrogen bonds with the main chain NH of Val899 in ZK1; and Arg699 in fingers1 forms hydrogen bonds with the side chain of Ser907 and the main chain oxygen of Leu905 in ZK1.

Fingers2 in CM interacts with the C-terminal region of ZK1 (Fig. 2B). Phe932 and Ile935 of ZK1 form hydrophobic interactions with Phe1202, Met1252, and Ile1256 of fingers2, while Met943 in ZK1 interacts hydrophobically with Leu1190, Leu951, and Phe947. Arg933 in ZK1 hydrogen bonds with the main chain oxygens of Glu1198 and Glu1199. The nc-palm in LIM also interacts with fingers2 via hydrophobic contacts: Phe1218 of fingers2 in CM inserts into a hydrophobic pocket formed by Pro426, Leu429, Ile430, Phe449, and Pro454 of nc-palm (Fig. 2C). Collectively, these protein–protein interactions position CM close to LIM, placing the

double-stranded stem pre-let-7 in the cleft between LIM and CM for efficient uridylylation as described below.

The structure also reveals direct interactions between the ZF in LIM of hTUT4 and the ZKs of hLin28A (Fig. 2D). Pro156 and Pro158 of hLin28A, located within the conserved PPQP motif between the two ZKs (Supplementary Fig. S7), form hydrophobic interactions with Gly276, Leu277, Ala280, and Ile316 in the ZF of hTUT4. Additionally, Gln317 of hTUT4_ZF hydrogen bonds with the main chain oxygen of Lys153 of hLin28A. To assess the functional importance of the hLin28A–hTUT4 interaction, we generated point mutants in the PPQP motif of hLin28A. Under the conditions used for the Lin28-dependent oligo-uridylylation of pre-let-7 by TUT4, around 30–40 uridines are added to the 3′-end of pre-let-7, as previously described (Supplementary Fig. S1) [11, 29]. The longer tails observed in the extended reaction likely result from a partially distributive elongation mechanism, in which hTUT4 can transiently unbind and re-bind to the oligo-uridylated RNA substrate, thereby enabling further extension in Lin28-indepenendet manner. The P155E/P156E and P158E mutations reduced Lin28A-dependent oligo-uridylation of pre-let-7, whereas the P155E/P156E/P158E triple mutation completely abolished it (Fig. 2F and G). We also prepared an hTUT4 truncation variant lacking the Lin28A-interacting region (hTUT4_281–1313), which similarly lost the ability to mediate oligo-uridylation. Taken together, these results indicate that the direct interaction between hLin28A and hTUT4 is crucial for Lin28A-dependent oligo-uridylation of pre-let-7, in addition to the interaction between hTUT4 and hLin28A mediated by pre-let-7 [29, 32].

## Recognition of pre-let-7g_UUU by hTUT4 and hLin28A

hTUT4 and hLin28A together extensively recognize pre-let-7_UUU through multiple RNA-binding domains (Fig. 3A–G). The fingers2 interacts with the region of the dsRNA stem distal to the preE loop (Fig. 3A and B). Lys1225 hydrogen bonds with the phosphate oxygen of A69, Arg1245 hydrogen bonds with the phosphate oxygen of C67 and the O3 atom of G66, and Lys1246 hydrogen bonds with the 2′-OH of G66. Additional hydrogen bonds are formed between the main chain oxygen of Gly1242 and the 2′-OH of C68, and between Ser1244 and the O2 atom of U12 (Fig. 2B). The ZK1 and fingers1 interact with the stem regions more proximal to the preE loop than fingers2 (Fig. 3A, C, and D). In ZK1, Lys919 hydrogen bonds with the phosphate oxygen of G66, Lys920 hydrogen bonds with the phosphate oxygen and the O4 atom of U14, and Asp921 hydrogen bonds with the 2′-OH of G15 (Fig. 3C). In fingers1, Arg669 hydrogen bonds with the 2′-OH of C63, and Arg670 hydrogen bonds with the phosphate oxygen of G65 (Fig. 3D). The ZF in LIM of hTUT4 interacts with the double-stranded stem of pre-let-7g, proximal to preE loop, and together with Lin28A, interacts with the single-stranded preE bulge containing the conserved 5′-GGAG-3′ motif (G50-G51-A52-G53) (Fig. 3A, E, F, and G). For dsRNA stem recognition by ZF, Lys321 and Lys330 hydrogen-bond with the phosphate oxygens of A19 and A17, respectively, while Glu325 and Arg327 hydrogen-bond with the 2′-OH of A17 and U16. For preE bulge recognition, Arg283, Lys324, Lys326, and Lys329 hydrogen-bond with the phosphate oxygens of A52, A54, U55, and A54, respectively, and His320 stacks on the adenine base of A52 (Fig. 3E and F). The ZK domains of hLin28A also specifically recognize the preE bulge. The main chain NH of Ala149 hydrogen bonds with the N7 atom of G53, the main chain oxygen of Gln157 hydrogen bonds with the N6 atom of A52, Lys159 hydrogen bonds with the phosphate oxygen of G51, the main chain oxygen of Lys160 hydrogen bonds with the N1 atom of G50, and the main chain NH of His162 hydrogen bonds with the O6 atom of G50 (Fig. 3E and F).

The RNA-interacting residues of hTUT4 are highly conserved across species (Supplementary Figs S6 and S7) and have been characterized in previous studies [29, 32, 33]. K321A/K324A, K326A/R327A, K329A/K330A mutations in ZF and R669A/R670A in fingers1 reduce ternary complex formation and hLin28A-dependent oligo-uridylylation [29]. While the R283A/R286A, H320A/K321A, and K324A/R327A mutations in ZF decrease hLin28A-dependent oligo-uridylylation, K919A/K920A mutation in ZK1 does not affect uridylylation. Since the RNA recognition involving fingers2 in CM had not been characterized, we generated mutants of the RNA-interacting residues in fingers2 of hTUT4 (Fig. 3H and I). Substitutions K1225E, R1245E, and K1246E reduced hLin28A-dependent oligo-uridylylation. The K1246E mutation would also block the Lin28-independent distributive elongation. Double and triple mutations (R1245E/K1246E and K1225E/R1245E/K1246E) abolished oligo-uridylylating activity. These results suggest that fingers2–RNA interactions are crucial for hLin28A-dependent oligo-uridylylation of pre-let-7 by hTUT4. Since these interactions do not contribute to initialpre-let-7 recognition by hTUT4 and hLin28A as described below, they may play a critical role in facilitating the oligo-uridylylation stage after the ternary complex has been formed.

## Structural comparison with hTUT7:hLin28A:pre-let7g complex

Recently, the cryo-EM structure of the hTUT7:hLin28A:pre-let-7g complex was reported (PDB ID: 8OPT; Fig. 4A–E) [33]. hTUT7 is a close paralog of hTUT4 and shares a similar domain composition (Fig. 1A). TUT4 and TUT7 exhibit comparable biochemical activities and function redundantly in pre-let-7 miRNA regulation. Consistent with these similarities, several common structural features were observed: the CM and LIM are located adjacent to each other; the ZKs of hLin28A recognize the GGAG motif in cooperation with the ZF of hTUT7; and the ZF, fingers1, and ZK1 together encircle the double-stranded stem of pre-let-7g (Fig. 4A and B).

A notable difference between the two structures is the relative orientation of domains in the complexes. In the superposition based on the ZFs of hTUT4 and hTUT7, the fingers2 domain is rotated by ∼30° (Fig. 4C). The hTUT4 complex adopts a more closed conformation, which is associated with additional contact between RNA and fingers2 (Fig. 4D and E), where the double-stranded region is stably clamped by the fingers2 in CM and fingers1 and ZF in LIM (Fig. 3A and B). Given the biochemical similarities of TUT4 and TUT7, this structural difference likely arises from the different RNA substrates used in the structural analyses: pre-let-7g with 1-nt 3′-overhang in the hTUT7 ternary complex and pre-let-7g with three additional 3′ uridines, pre-let-7g_UUU, in the hTUT4

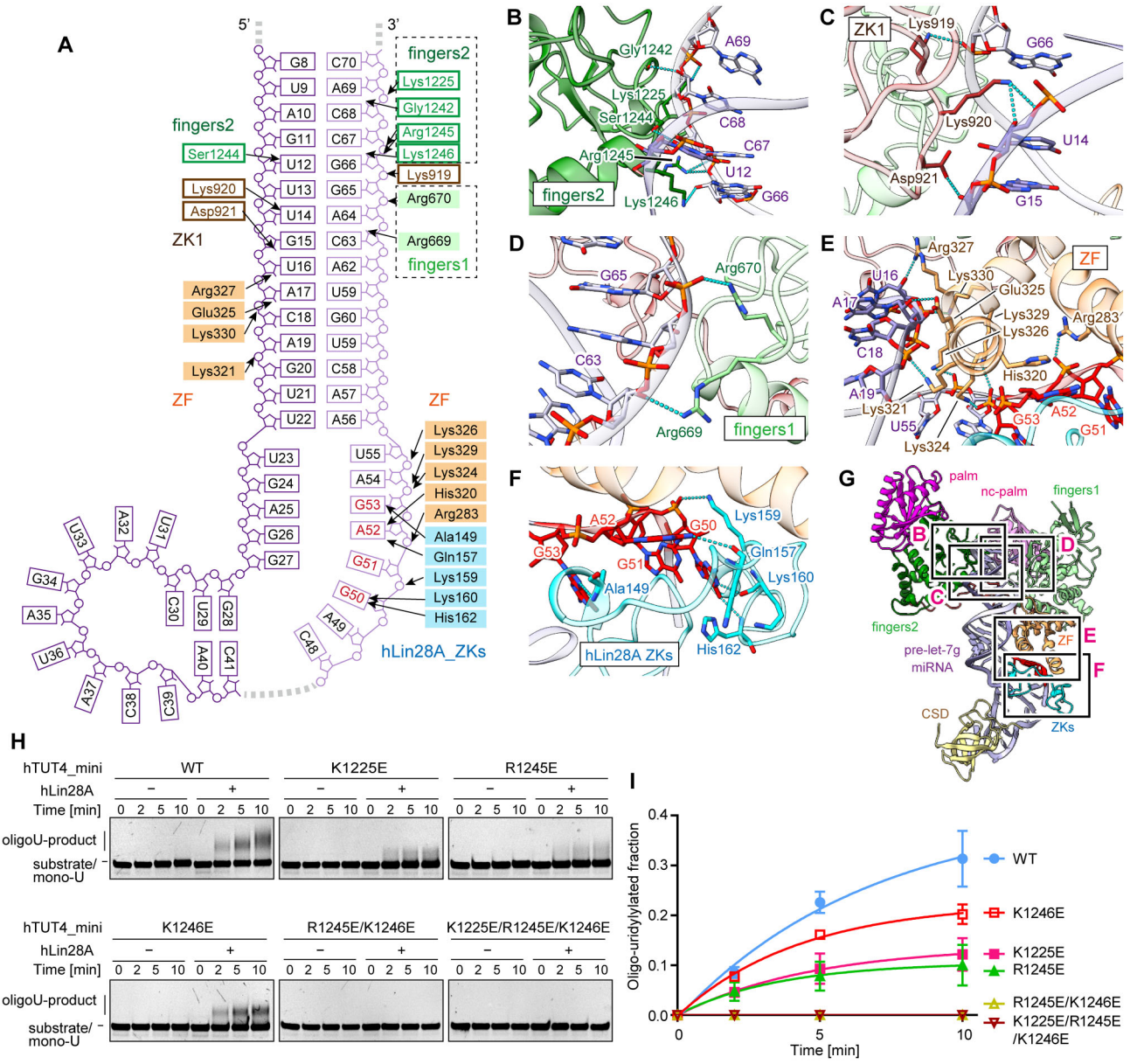


**Figure 3.** Interactions between hTUT4, hLin28A, and pre-let-7g_UUU. (**A**) Schematic representation of pre-let-7g miRNA interactions with hTUT4_mini and hLin28A. (**B–F**) Detailed views of RNA recognition by hTUT4: (B) fingers2, (C) ZK1, (D) fingers1, and (E, F) ZF, along with ZKs of hLin28A. (**G**) Cartoon representation of the overall complex, with regions corresponding to panels (B–F) indicated. (**H**) *In vitro* oligo-uridylylation of pre-let-7a-1 RNA by hTUT4_mini or its variants. Substrate RNA (250 nM) was incubated with hTUT4_mini or variants (20 nM) and 1 mM UTP at 37°C, in the presence or absence of hLin28A (500 nM). (**I**) Quantification of uridylation activity from (H). Data represent mean ± SD ($n = 3$).

ternary complex. The hTUT7 ternary complex in an open conformation likely represents the initial uridylylation stage, whereas the hTUT4 ternary complex in a closed conformation may represent a state after the addition of several uridines, the elongation stage.

Both in the hTUT4 and TUT7 ternary complexes, the cryo-EM densities corresponding to the 3′- and 5′-terminal region of the pre-let-7g are not visible (Fig. 4A and B), indicating the flexibility or heterogeneity of the regions. The CSD of hLin28A is modeled in the hTUT4 ternary complex but not in the hTUT7 complex. Given the suboptimal map quality in this region, the discrepancy may result from differences in model-building criteria or particle selection strategies during cryo-EM data processing.

## Requirements of structural features of pre-let-7 for uridylylation

The 5′ and 3′ terminal regions of pre-let-7 were not modeled in the hTUT4:hLin28A:pre-let-7g_UUU structure (Figs 1B, C, and 4A) due to the absence of the corresponding cryo-EM density maps.

In the current hTUT4_mini:Lin28A:pre-let-7g_UUU structures, the orientation of the dsRNA does not point toward the catalytic site (Fig. 1C, D), suggesting that structural rearrangements of the RNA, the proteins, or both are required for uridylylation at the catalytic site in CM (Supplementary Fig. S8A). One possible model is that the 5′ and 3′ terminal parts of the stem region of pre-let-7 become destabilized or unwound, without dissociation of the CM from the LIM or of fingers2

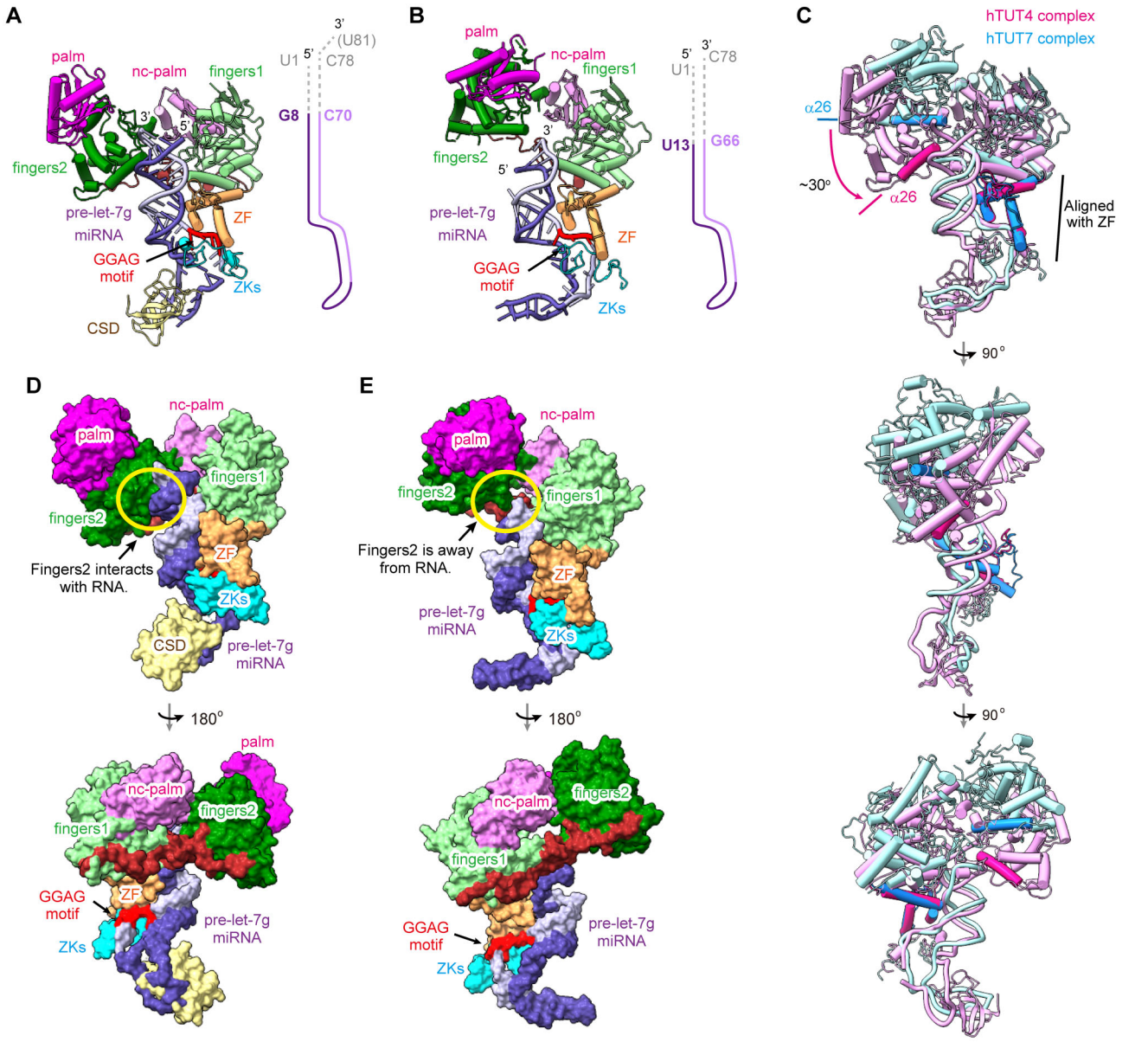


**Figure 4.** Structural comparison between hTUT4_mini:hLin28A:pre-let-7g_UUU and hTUT7:hLin28A:pre-let-7g. (**A, B**) Cryo-EM structures of (A) hTUT4_mini:hLin28A:pre-let-7g_UUU and (B) hTUT7:hLin28A:pre-let-7g (PDB ID: 8OPT) [33]. Schematic diagrams of pre-let-7g_UUU and pre-let-7g are shown on the right; the 5′ and 3′ halves are colored purple and light purple, respectively, with unmodeled regions in gray. (**C**) Structural superposition of the hTUT4 complex (magenta) and hTUT7 complex (cyan), aligned by the ZF domains. Fingers2 in the CM adopts a ∼30° different orientation relative to the ZFs. For clarity, ZFs and α26 helices in fingers2 of hTUT7 and hTUT4 are highlighted in blue and red, respectively. (**D, E**) Surface representations of the structures of (D) hTUT4_mini:hLin28A:pre-let-7g_UUU and (E) hTUT7:hLin28A:pre-let-7g.

in the CM from the stem region of pre-let-7, thereby allowing the 3′ end of pre-let-7 to relocate into the catalytic pocket (Supplementary Fig. S8B). Another model is that the CM relocates to the 3′ end of the extended double-stranded stem to initiate oligo-uridylylation (Supplementary Fig. S8C). In this scenario, the CM dissociates from LIM in the current complex and consecutively uridylylates the 3′-end of pre-let-7g.

To gain insight into hTUT4/hLin28A-mediated oligo-uridylylation, we tested *in vitro* uridylylation of wild-type pre-let-7a-1 and a series of its variants (Fig. 5A–E, Supplementary Fig. S9): two with stabilized terminal base pairs (tight-A, U67C/U70C; tight-B, U1G/U70C/U71C); two with destabilized terminal base pairs (loose-A, C68A/U69C; loose-B, G66C/U68A/C68A/U69C); a deletion of the 5′ seven nucleotides (del_1–7); and variants with deletions or insertions in the double-stranded stem (del_4bp, del_6bp, del_8bp, and ins_4bp). hTUT4 efficiently oligo-uridylylated wild-type pre-let-7a-1 in a Lin28A-dependent manner, as well as the loose-A, loose-B, and del_1–7 variants, indicating that these mutations have little effect on oligo-uridylylation. In contrast, the tight-A and tight-B variants were not oligo-uridylylated, suggesting that destabilization of the terminal base pair is required for hLin28A-dependent oligo-uridylylation. In these stabilized RNAs, the terminal region may fail to destabilize sufficiently within the complex, preventing the 3′ end from relocating into the catalytic pocket in CM (Fig. 5E). While the del_4bp variant was oligo-uridylylated with comparable or slightly reduced efficiency relative to wild-type pre-

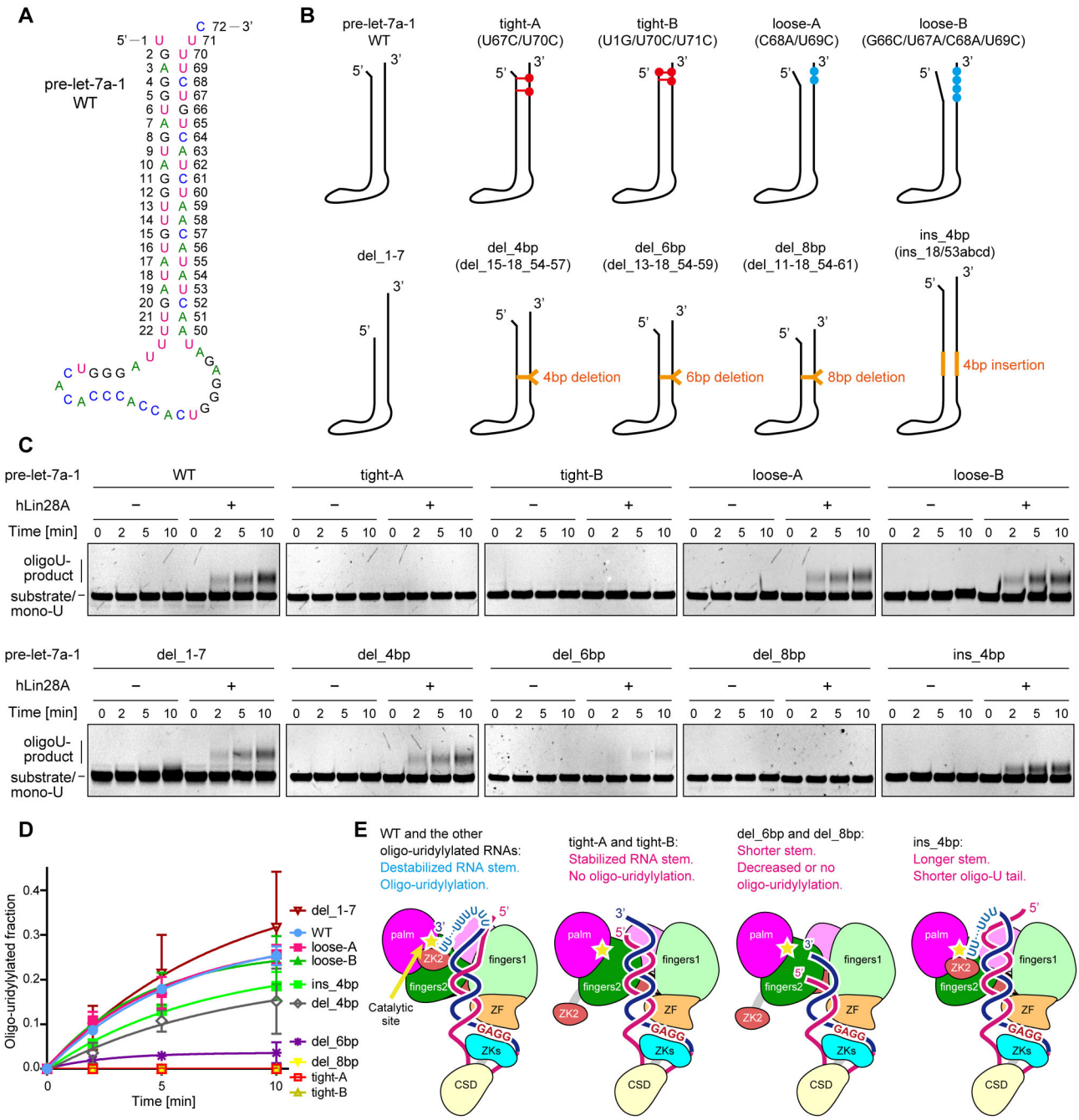


**Figure 5.** *In vitro* oligo-uridylylation of pre-let-7a variants by hTUT4 in the presence of hLin28A. (**A**) Predicted secondary structure of wild-type (WT) pre-let-7a-1. Nucleotides are colored as follows: adenine (green), guanine (black), cytosine (cyan), and uracil (magenta). (**B**) Schematic of engineered pre-let-7a-1 variants. Mutations predicted to strengthen or weaken base pairing are shown in red or cyan, respectively. Deletions and insertions are indicated in orange. (**C**) *In vitro* oligo-uridylylation assay using WT and mutant pre-let-7a-1 RNAs. Substrates (250 nM) were incubated with hTUT4_mini (20 nM) and UTP (1 mM) at 37°C in the presence or absence of hLin28A (500 nM). (**D**) Quantification of uridylylation activity from (C). Data represent mean ± SD ($n = 2$). (E) Schematic model proposing a mechanistic explanation for differences in oligo-uridylylation efficiency among variants.

let-7a-1, the del_6bp and del_8bp variants exhibited progressively diminished or abolished hLin28A-dependent oligo-uridylylation, respectively. This length-dependent decrease suggests that a sufficient stem length from the preE region is required for accommodation of the 3′ end of pre-let-7 into the catalytic site of the CM (Fig. 5E). The ins_4bp variant was also efficiently oligo-uridylylated, but the oligouridine tails were shorter than those of wild-type pre-let-7 (Fig. 5C). This is likely because, compared with the normal stem length of pre-let-7, the oligo-uridylylated products can occupy the catalytic site with fewer uridines, thereby limiting further elongation.

Taken together, our structural and biochemical analyses imply that hLin28A-dependent oligo-uridylylation of pre-let-7 requires destabilization of the terminal base pairs in the double-stranded stem to permit accommodation of the 3′ end into the catalytic site of the CM, and the CM–LIM interaction would be retained during oligo-uridylylation as described below.

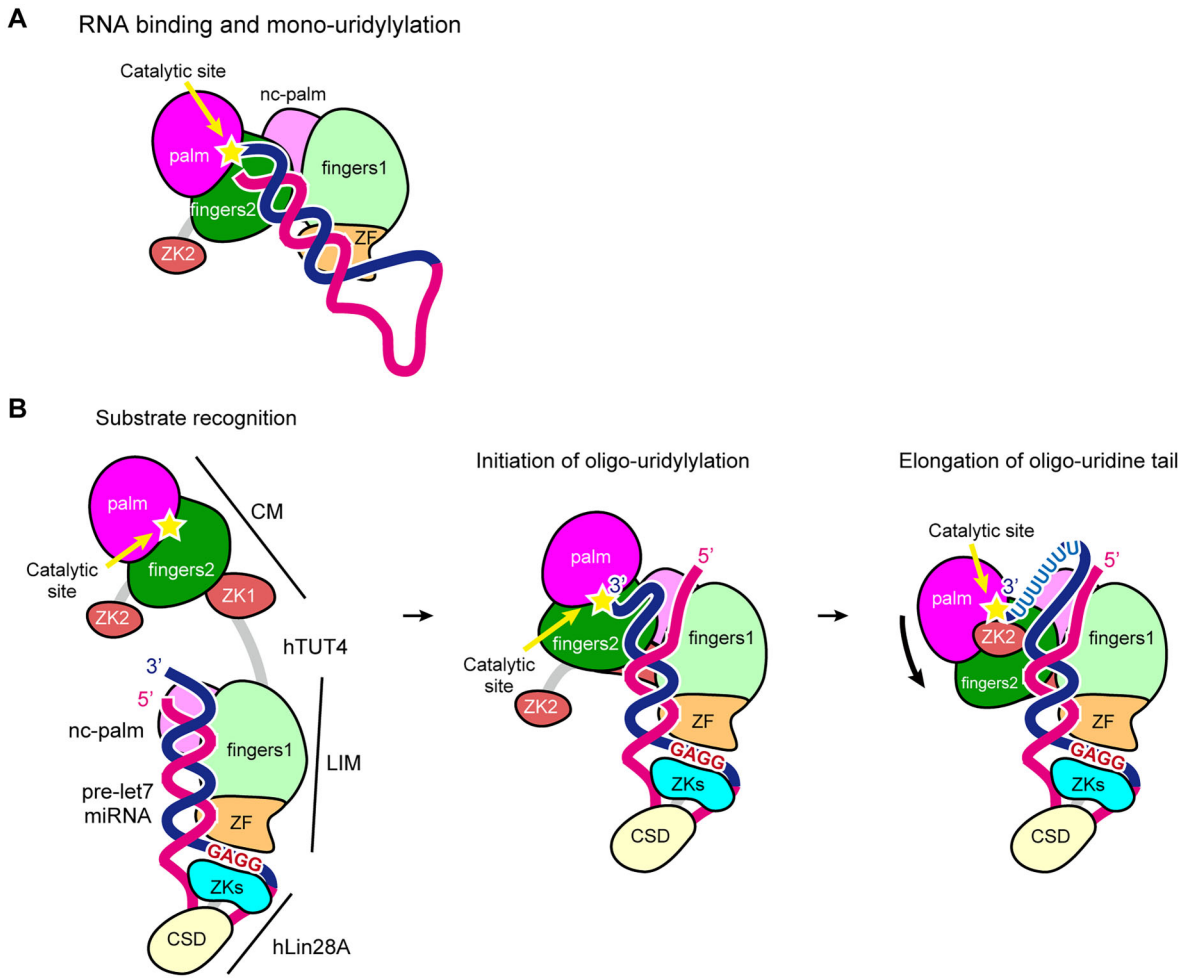


**Figure 6.** Mono- and oligo-uridylylation of pre-let-7 by hTUT4. (**A**) Schematic of mono-uridylylation of class I pre-let-7 miRNA by hTUT4. Domains of hTUT4 are colored as follows: ZF (orange), nc-palm (light magenta), fingers1 (light green), ZK (brown), palm (magenta), and fingers2 (green). hLin28A CSD and ZK are shown in yellow and cyan. Pre-let-7 is depicted with 5′-half in red and 3′-half in blue. In the absence of hLin28A, hTUT4 binds pre-let-7 with a 1-nt 3′ overhang and adds a single uridine to facilitate further processing. (**B**) Schematic of oligo-uridylylation in the presence of hLin28A. (left panel) Substrate recognition complex forms via hTUT4_LIM, hLin28A, and pre-let-7. (middle panel) The CM module engages the 3′ end, destabilizing the upper stem and initiating oligo-uridylylation (initiation stage). (right panel) During elongation, fingers2 in CM clamps the stem region, stabilizing the complex, and ZK2 interacts with oligo-uridine tail for processive oligo-uridylylation.

## Discussion

In this study, we determined the cryo-EM structure of the hTUT4:hLin28A:pre-let-7g_UUU ternary complex (Fig. 1), which provides mechanistic insights into Lin28A-dependent oligo-uridylylation of pre-let-7. The structure revealed that the double-stranded stem of pre-let-7g is clamped within a cleft formed by the LIM and CM of hTUT4, with the 5′-GGAG-3′ motif in the pre-E jointly recognized by the ZKs of hLin28A and the ZF of hTUT4 (Fig. 3). In addition to RNA-mediated interactions, a direct protein–protein contact between the PPQP motif of hLin28A and the ZF of hTUT4 was observed (Fig. 2D), and consistently the interaction is indispensable for efficient uridylylation (Fig. 2F andG), highlighting the cooperative nature of RNA- and protein-mediated recognition in ternary complex assembly.

Comparison with the recently reported hTUT7:hLin28A:pre-let-7g structure, in which pre-let-7g has 1-nt 3′-overhang, underscores both the redundancy and distinct conformational states of TUT4 and TUT7 (Fig. 4). Although both complexes share common RNA recognition modes, the CM, in hTUT4 adopts a more closed orientation relative to hTUT7, accompanied by additional contacts between fingers2 in CM and the dsRNA stem distal to the pre-E loop (Figs 1C, 3B, 4). Consistently, the interactions between fingers2 and dsRNA stem are required for efficient uridylylation (Fig. 3H and I). Given the biochemical redundancy between TUT4 and TUT7, this structural difference likely arises from the status of 3′-end of pre-let-7g and pre-let-7g_UUU, and reflects distinct catalytic stages captured in the cryo-EM studies: the open conformation of hTUT7:hLin28A:pre-let-7g represents an early, pre-elongation stage (or an initiation stage), whereas the closed conformation of hTUT4_mini:hLin28A:pre-let-7g_UUU corresponds to an elongation stage following the addition of several uridines (Fig. 6).

The mutants of pre-let-7 with stabilized terminal base pairs could not be oligo-uridylylated, while those of destabilized base pairs or 5′-deletion remained uridylylated as wild-type pre-let-7 (Fig. 5A–C). This observation implies that the stem region of pre-let-7 is intrinsically weak and is related to the 5′ strand of the miRNA duplex to be preferentially incorpo-

rated into Argonaute proteins [44, 45]. In the pre-let-7 family, 5′-terminal uridines remain unpaired or form base pairs with G or A, and the 5′-second guanines from base pairs with U (Fig. 5A, Supplementary Fig. S11). The upper portion of the dsRNA stem frequently contains G–U wobble base pairs, and the upper six base pairs often include additional G–U pairs and/or mismatches (Supplementary Fig. S11). Considering the presence of unpaired or weakly paired nucleotides of the stem, as well as the thermodynamic instability of G–U wobble pairs—particularly their propensity to fray at terminal positions—and their structural deviations such as local distortions or helical shifts [46, 47], the upper part of the stem may have an intrinsic tendency toward transient unwinding. Furthermore, binding of TUT4 to the lower region of the stem may impose conformational strain, which could further promote partial destabilization of the upper dsRNA region. Even pre-let-7 with a longer stem could be oligo-uridylylated, but the number of uridines added decreased (Fig. 5B–D). These results imply that the length and stability of the stem of pre-let-7 are required for the efficient oligo-uridylation (Fig. 5E).

In both structures of hTUT7:hLin28A:pre-let-7g and hTUT4_mini:hLin28A:pre-let-7g_UUU, the 5′- and 3′-parts of pre-let-7g were not visible due to the absence of corresponding cryo-EM density maps (Figs 1C, D, and 4). Together with the requirement for optimal stem length and stability, these observations suggest that the upper part of pre-let-7 is unwound, allowing the 3′ end to be relocated into the CM's catalytic pocket. This model contrasts with a scenario in which the CM dissociates from the LIM and is separately recruited to the extended 3′ end during oligo-uridylylation (Supplementary Fig. S8). Consistently, deletion of the flexible linker between the CM and LIM does not reduce the oligo-uridylation of pre-let-7, suggesting that the association between CM and LIM is maintained during oligo-uridylylation (Supplementary Fig. S10).

In summary, the Lin28-dependent mechanism of pre-let-7 uridylylation by hTUT4 involves distinct steps that regulate the transition between mono- and oligo-uridylylation (Fig. 6). In the absence of Lin28A, hTUT4 alone accommodates pre-let-7 with a 1-nt 3′ overhang and adds a single uridine, generating a 2-nt overhang, which is then released from TUT4, thereby promoting efficient Dicer processing. In the presence of Lin28A, hTUT4 and Lin28A cooperatively bind pre-let-7, with the CM initially being mobile. The recruitment of CM to the complex via protein–protein interactions with LIM, together with destabilization of the terminal base pairs, allows the 3′ end of pre-let-7 to access the catalytic pocket and initiate uridylylation. During elongation, interactions between fingers2 and the RNA stem stabilize the closed conformation of CM, supporting the addition of multiple uridines. ZK2 in CM interacts with the oligo-uridine tail, enabling efficient oligo-uridylylation [30]. The growing oligo-uridine tail eventually creates steric hindrance in the catalytic pocket, disrupting the complex and terminating the reaction.

These structural and mechanistic insights show that Lin28A-dependent pre-let-7 oligo-uridylation is a highly regulated process coordinated with RNA structure and protein–protein interactions. This mechanism precisely controls miRNA biogenesis, affecting let-7 expression during development, stem cell maintenance, and tumorigenesis [5]. The cooperative action of TUT4/TUT7 and Lin28A also modulates precursor miRNA processing by Dicer, highlighting its impact on gene expression networks and potential as a target for stem cell and cancer research.

## Acknowledgements

We thank the staff of the Cryo-electron Microscopy Facility at the University of Tokyo for technical assistance during data collection.

*Author contributions*: Xiaojie Han (Data curation [equal], Formal analysis [equal], Investigation [equal], Writing—original draft [equal]), Seisuke Yamashita (Data curation [equal], Formal analysis [equal], Investigation [equal], Validation [equal], Writing—original draft [equal]), and Kozo Tomita (Conceptualization [lead], Data curation [equal], Formal analysis [equal], Funding acquisition [lead], Investigation [lead], Project administration [lead], Supervision [lead], Validation [equal], Writing—original draft [equal], Writing—review & editing [lead]).

## Supplementary data

Supplementary data is available at NAR online.

## Conflict of interest

None declared.

## Funding

This work was supported by the Funding Program for Next Generation World-Leading Researchers of JSPS [grant number LS135 to K.T.], Grants-in-Aid for Scientific Research (A) [grant numbers 23H00368, 18H03980, and 26251009 to K.T.], and a Grant-in-Aid for Scientific Research on Innovative Areas from the Ministry of Education, Culture, Sports, Science, and Technology of Japan [grant number 26113002 to K.T.]. K.T. was also supported by grants from the Uehara Memorial Foundation, the Terumo Foundation for Life Science and Art, and the Princess Takamatsu Cancer Research Fund. Cryo-EM data collection was supported by the Research Support Project for Life Science and Drug Discovery [Basis for Supporting Innovative Drug Discovery and Life Science Research (BINDS)] from AMED under grant number JP23ama121002. Funding to pay the Open Access publication charges for this article was provided by JSPS.

## Data availability

The atomic coordinates of the hTUT4:hLin28A:pre-let-7g_UUU complex have been deposited in the Protein Data Bank (PDB 9W4R and 9W4S for complexes 1 and 2, respectively). The EM maps for complexes 1 and 2 have been deposited in the Electron Microscopy Data Bank (EMD-65642 and EMD-65643, respectively).

## References

1. Lee RC, Ambros V. An extensive class of small RNAs in *Caenorhabditis elegans*. *Science* 294:862–4.
2. Pasquinelli AE, Reinhart BJ, Slack F *et al.* Conservation of the sequence and temporal expression of let-7 heterochronic regulatory RNA. *Nature* 2000;408:86–9. https://doi.org/10.1038/35040556

3. Roush S, Slack FJ. The let-7 family of microRNAs. *Trends Cell Biol* 2008;18:505–16. https://doi.org/10.1016/j.tcb.2008.07.007
4. Bussing I, Slack FJ, Grosshans H. let-7 microRNAs in development, stem cells and cancer. *Trends Mol Med* 2008;14:400–9. https://doi.org/10.1016/j.molmed.2008.07.001
5. Thornton JE, Gregory RI. How does Lin28 let-7 control development and disease? *Trends Cell Biol* 2012;22:474–82. https://doi.org/10.1016/j.tcb.2012.06.001
6. Balzeau J, Menezes MR, Cao SY *et al.* The Lin28/let-7 pathway in cancer. *Front Genet* 2017;8:31. https://doi.org/10.3389/fgene.2017.00031
7. Lee Y, Kim M, Han J *et al.* MicroRNA genes are transcribed by RNA polymerase II. *EMBO J* 2004;23:4051–60. https://doi.org/10.1038/sj.emboj.7600385
8. Basyuk E, Suavet F, Doglio A *et al.* Human let-7 stem-loop precursors harbor features of RNase III cleavage products. *Nucleic Acids Res* 2003;31:6593–7. https://doi.org/10.1093/nar/gkg855
9. Yi R, Qin Y, Macara I *et al.* Exportin-5 mediates the nuclear export of pre-microRNAs and short hairpin RNAs. *Genes Dev* 2003;17:3011–6. https://doi.org/10.1101/gad.1158803
10. Wilczynska A, Bushell M. The complexity of miRNA-mediated repression. *Cell Death Differ* 2015;22:22–33. https://doi.org/10.1038/cdd.2014.112
11. Heo I, Joo C, Cho J *et al.* Lin28 mediates the terminal uridylation of let-7 precursor microRNA. *Mol Cell* 2008;32:276–84. https://doi.org/10.1016/j.molcel.2008.09.014
12. Heo I, Joo C, Kim Y-K *et al.* TUT4 in concert with Lin28 suppresses microRNA biogenesis through pre-microRNA uridylation. *Cell* 2009;138:696–708. https://doi.org/10.1016/j.cell.2009.08.002
13. Hagan JP, Piskounova E, Gregory RI. Lin28 recruits the TUTase Zcchc11 to inhibit let-7 maturation in mouse embryonic stem cells. *Nat Struct Mol Biol* 2009;16:1021–U1033. https://doi.org/10.1038/nsmb.1676
14. Thornton JE, Chang H-M, Piskounova E *et al.* Lin28-mediated control of let-7 microRNA expression by alternative TUTases Zcchc11 (TUT4) and Zcchc6 (TUT7). *RNA* 2012;18:1875–85. https://doi.org/10.1261/rna.034538.112
15. Heo I, Ha M, Lim J *et al.* Mono-uridylation of pre-microRNA as a key step in the biogenesis of group II let-7 microRNAs. *Cell* 2012;151:521–32. https://doi.org/10.1016/j.cell.2012.09.022
16. Kim B, Ha M, Loeff L *et al.* TUT7 controls the fate of precursor microRNAs by using three different uridylation mechanisms. *EMBO J* 2015;34:1801–15. https://doi.org/10.15252/embj.201590931
17. Stevenson AL, Norbury CJ. The Cid1 family of non-canonical poly(A) polymerases. *Yeast* 2006;23:991–1000. https://doi.org/10.1002/yea.1408
18. Martin G, Keller W. RNA-specific ribonucleotidyl transferases. *RNA* 2007;13:1834–49. https://doi.org/10.1261/rna.652807
19. Yashiro Y, Tomita K. Function and regulation of human terminal uridylyltransferases. *Front Genet* 2018;9:538.https://doi.org/10.3389/fgene.2018.00538
20. Yamashita S, Takagi Y, Nagaike T *et al.* Crystal structures of U6 snRNA-specific terminal uridylyltransferase. *Nat Commun* 2017;8:15788.https://doi.org/10.1038/ncomms15788
21. Yamashita S, Tomita K. Cryo-EM structure of human TUT1:U6 snRNA complex. *Nucleic Acids Res* 2025;53. https://doi.org/10.1093/nar/gkae1314
22. Faehnle CR, Walleshauser J, Joshua-Tor L. Mechanism of Dis3l2 substrate recognition in the Lin28-let-7 pathway. *Nature* 2014;514:252–6. https://doi.org/10.1038/nature13553
23. Ustianenko D, Hrossova D, Potesil D *et al.* Mammalian DIS3L2 exoribonuclease targets the uridylated precursors of let-7 miRNAs. *RNA* 2013;19:1632–38. https://doi.org/10.1261/rna.040055.113
24. Chang H-M, Triboulet R, Thornton JE *et al.* A role for the Perlman syndrome exonuclease Dis3l2 in the Lin28-let-7 pathway. *Nature* 2013;497:244–8. https://doi.org/10.1038/nature12119
25. Loughlin FE, Gebert LFR, Towbin H *et al.* Structural basis of pre-let-7 miRNA recognition by the zinc knuckles of pluripotency factor Lin28. *Nat Struct Mol Biol* 2012;19:84–89. https://doi.org/10.1038/nsmb.2202
26. Nam Y, Chen C, Gregory RI *et al.* Molecular basis for interaction of let-7 MicroRNAs with Lin28. *Cell* 2011;147:1080–91. https://doi.org/10.1016/j.cell.2011.10.020
27. Wang L, Rowe RG, Jaimes A *et al.* Small-molecule inhibitors disrupt let-7 oligouridylation and release the selective blockade of let-7 processing by Lin28. *Cell Rep* 2018;23:3091–101. https://doi.org/10.1016/j.celrep.2018.04.116
28. Ustianenko D, Chiu HS, Treiber T *et al.* LIN28 selectively modulates a subclass of let-7 microRNAs. *Mol Cell* 2018;71:271–83. https://doi.org/10.1016/j.molcel.2018.06.029
29. Yamashita S, Nagaike T, Tomita K. Crystal structure of the Lin28-interacting module of human terminal uridylyltransferase that regulates let-7 expression. *Nat Commun* 2019;10:1960. https://doi.org/10.1038/s41467-019-09966-5
30. Faehnle CR, Walleshauser J, Joshua-Tor L. Multi-domain utilization by TUT4 and TUT7 in control of let-7 biogenesis. *Nat Struct Mol Biol* 2017;24:658–65. https://doi.org/10.1038/nsmb.3428
31. Wang L, Nam Y, Lee AK *et al.* LIN28 zinc knuckle domain is required and sufficient to induce let-7 oligouridylation. *Cell Rep* 2017;18:2664–75. https://doi.org/10.1016/j.celrep.2017.02.044
32. Faehnle CR, Walleshauser J, Joshua-Tor L. Multi-domain utilization by TUT4 and TUT7 in control of let-7 biogenesis. *Nat Struct Mol Biol* 2017;24:658–65. https://doi.org/10.1038/nsmb.3428
33. Yi G, Ye M, Carrique L *et al.* Structural basis for activity switching in polymerases determining the fate of let-7 pre-miRNAs. *Nat Struct Mol Biol* 2024;31:1426–38. https://doi.org/10.1038/s41594-024-01357-9
34. Price SR, Ito N, Oubridge C *et al.* Crystallization of RNA-protein complexes. I. Methods for the large-scale preparation of RNA suitable for crystallographic studies. *J Mol Biol* 1995;249:398–408. https://doi.org/10.1006/jmbi.1995.0305
35. Kao C, Zheng M, Rüdisser S. A simple and efficient method to reduce nontemplated nucleotide addition at the 3 terminus of RNAs transcribed by T7 RNA polymerase. *RNA* 1999;5:1268–72. https://doi.org/10.1017/S1355838299991033
36. Punjani A, Rubinstein JL, Fleet DJ *et al.* cryoSPARC: algorithms for rapid unsupervised cryo-EM structure determination. *Nat Methods* 2017;14:290–6. https://doi.org/10.1038/nmeth.4169
37. Rubinstein JL, Brubaker MA. Alignment of cryo-EM movies of individual particles by optimization of image translations. *J Struct Biol* 2015;192:188–95. https://doi.org/10.1016/j.jsb.2015.08.007
38. Punjani A, Zhang H, Fleet DJ. Non-uniform refinement: adaptive regularization improves single-particle cryo-EM reconstruction. *Nat Methods* 2020;17:1214–21. https://doi.org/10.1038/s41592-020-00990-8
39. He J, Li T, Huang SY. Improvement of cryo-EM maps by simultaneous local and non-local deep learning. *Nat Commun* 2023;14:3217. https://doi.org/10.1038/s41467-023-39031-1
40. Jumper J, Evans R, Pritzel A *et al.* Highly accurate protein structure prediction with AlphaFold. *Nature* 2021;596:583–9. https://doi.org/10.1038/s41586-021-03819-2
41. Emsley P, Cowtan K. Coot: model-building tools for molecular graphics. *Acta Crystallogr Sect D-Biol Crystallogr* 2004;60:2126–32. https://doi.org/10.1107/S0907444904019158
42. Afonine PV, Grosse-Kunstleve RW, Echols N *et al.* Towards automated crystallographic structure refinement with phenix.refine. *Acta Crystallogr Sect D-Biol Crystallogr* 2012;68:352–67. https://doi.org/10.1107/S0907444912001308
43. Meng EC, Goddard TD, Pettersen EF *et al.* UCSF ChimeraX: tools for structure building and analysis. *Protein Sci* 2023;32:e4792. https://doi.org/10.1002/pro.4792
44. Hu HY, Yan Z, Xu Y *et al.* Sequence features associated with microRNA strand selection in humans and flies. *Bmc Genomics*

*[Electronic Resource]* 2009;10:413. https://doi.org/10.1186/1471-2164-10-413
45. Medley JC, Panzade G, Zinovyeva AY. microRNA strand selection: unwinding the rules. *Wiley Interdiscip Rev RNA* 2021;12:e1627. https://doi.org/10.1002/wrna.1627
46. Masquida B, Westhof E. On the wobble GoU and related pairs. *RNA* 2000;6:9–15. https://doi.org/10.1017/S1355838200992082
47. Varani G, McClain WH. The G x U wobble base pair. A fundamental building block of RNA structure crucial to RNA function in diverse biological systems. *EMBO Rep* 2000;1:18–23. https://doi.org/10.1093/embo-reports/kvd001



**Received:** September 22, 2025. **Revised:** November 23, 2025. **Accepted:** November 26, 2025